ROYAL SOCIETY
OF CHEMISTRY

PAPER

Check for updates

MXene-based multifunctional smart fibers for wearable and portable electronics†

Leiqiang Qin, [iD] ‡*a Jianxia Jiang,‡ab Lintao Hou, [iD] c Fengling Zhanga and Johanna Rosen*a

Fiber type devices are promising for applications in wearable and portable electronics. However, scalable fabrication of fiber electrodes with multifunctional performance for use in distinct fields remains challenging. Herein, high performance smart fibers based on $Mo_{1.33}C$ *i*-MXene nanosheets and poly(3,4-ethylenedioxythiophene):polystyrene sulfonate hybrid paste are fabricated with an easily scalable spinning approach. The hybrid fibers produced by this method can be applied in both high-performance supercapacitors and electrochemical transistors (ECTs). When assembled into a fiber type asymmetric supercapacitor with reduced graphene oxide (rGO) fiber, a capacitance of 105 F g^{-1} and an energy density of 37 mW h g^{-1} were reached for a potential window of 1.6 V. The hybrid fiber based ECT shows high transconductance and fast response time. This work demonstrates the potential of *i*-MXene-based fiber electrodes for multifunctional applications, to aid in the development of the next-generation, high-performance wearable electronic devices.

Introduction

Fiber-type opto-electronic components such as solar cells,[1–3] supercapacitors,[4] batteries[5] and transistors[6–8] with nonplanar device architectures have received significant attention for convenient integration into 'smart' fabrics. Important recent advances in fiber-type devices have exploited novel active materials. In particular, compared to their bulk counterparts, two-dimensional (2D) nanomaterials with fascinating properties and easily assembled structures in the form of nanoscale frameworks are building blocks for textile devices.[9–13] Until now, a growing number of 2D materials have garnered considerable attention for developing into macroscopic fibrous structures, including carbon nanotubes (CNTs),[14–16] reduced graphene oxide (rGO),[17–21] transition metal dichalcogenides (TMDs),[22] and metal oxides.[23–25] For example, significant progress has been made in development of one-dimensional (1D) carbon-based fibers prepared from CNTs or graphene oxides (GO). Carbon-based fibers possess outstanding physical and chemical properties, such as excellent electrical and thermal conductivities and high flexibility, mechanical strength, and chemical

stabilities, meeting the demands of the next generation of smart electronic devices woven into textiles.[26] However, compared to their corresponding film morphology, the properties of carbon-based fibers are significantly reduced. Especially for carbon-based micro-supercapacitors it remains challenging to achieve a high capacitance since the large specific surface area of the nanomaterial is not effectively utilized due to restacking of the nanosheets. In addition, insufficient attention has been paid to development of multifunctional fibers, which could be achieved through rational design by selecting suitable materials or combining two materials with different functionalities.

MXenes, as a growing family of 2D transition metal carbides and nitrides with excellent conductivity, mechanical strength, and potential for a wide range of applications, have been extensively explored.[27–33] MXenes are typically obtained by selectively etching the A layers in the atomically laminated $M_{n+1}AX_n$ phases,[34,35] where M is a transition metal, A is an A-group element, X is C and/or N. In particular, the pseudocapacitive charge storage mechanism and the increased surface area upon delamination of the multilayered MXene into single or few layers facilitates capacitance values superior to carbon materials. In 2017, we reported a new type of quaternary *i*-MAX phases, $(Mo_{2/3}Sc_{1/3})_2AlC$ and $(Mo_{2/3}Y_{1/3})_2AlC$, with two different M elements which are in-plane chemically ordered.[36] The first in-plane vacancy ordered *i*-MXene, $Mo_{1.33}C$, was prepared by selective removal of both the Al and Sc atoms from $(Mo_{2/3}Sc_{1/3})_2AlC$. The ordering of the vacancies together with a high conductivity enabled $Mo_{1.33}C$ with one of the highest volumetric capacitances (≈ 1150 F cm^{-3}) reported to date for a film electrode based on a 2D material. Furthermore, by post

aDepartment of Physics, Chemistry and Biology (IFM), Linköping University, Linköping, SE-58183, Sweden. E-mail: leiqiang.qin@liu.se; johanna.rosen@liu.se

bFlexible Electronics Innovation Institute, Jiangxi Science and Technology Normal University, Nanchang, 330013, China

cGuangzhou Key Laboratory of Vacuum Coating Technologies and New Energy Materials, Physics Department, Jinan University, Guangzhou, 510632, China

† Electronic supplementary information (ESI) available. See https://doi.org/10.1039/d2ta01428a
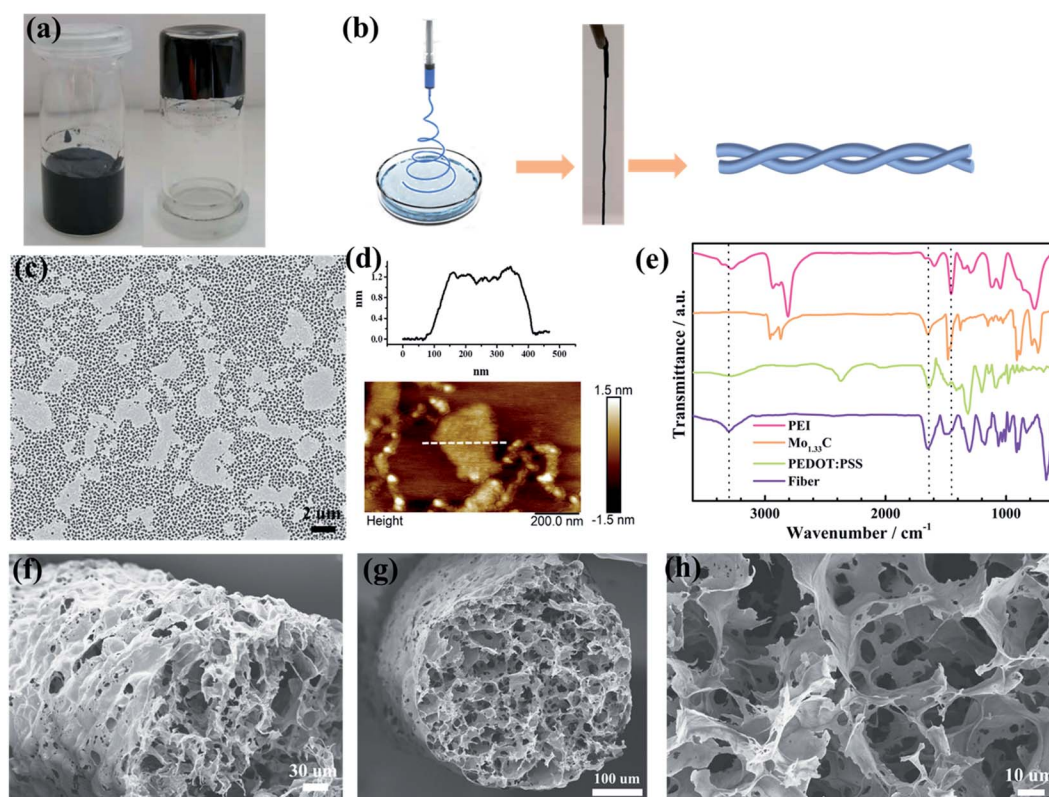
‡ Leiqiang Qin and Jianxia Jiang contributed equally to this work.

Fig. 1 Preparation of *i*-MXene fiber. (a) Optical image of $Mo_{1.33}C$/PEDOT:PSS hybrid paste. (b) Schematic illustration of the preparation of *i*-MXene fiber. (c) $Mo_{1.33}C$ *i*-MXene single layer coated on an Al_2O_3 filter paper. (d) AFM image of $Mo_{1.33}C$ single sheets and hight-line profile. (e) FT-IR spectra of PEI, $Mo_{1.33}C$, PEDOT:PSS and fiber. (f) SEM image of the hybrid fiber surface. (g and h) SEM images of cross-section of hybrid fiber at different magnifications.

etching treatment of the electrode, or by combining the *i*-MXene with conducting polymer poly(3,4-ethylenedioxythiophene):polystyrene sulfonate (PEDOT:PSS), a higher capacitive performance can be achieved for electrodes based on MXene only and composite film electrode architectures, respectively.[37,38] However, film electrodes obtained by traditional electrode fabrication methods suffer severe performance degradation for thick films or high rates.

Herein, we present the design and fabrication of flexible and efficient MXene based multifunctional smart fibers through a straightforward and scalable synthetic route using $Mo_{1.33}C$/PEDOT:PSS hybrid paste where PEDOT:PSS as a conductive binder promotes spinnability and flexibility as well as an increased interlayer spacing between $Mo_{1.33}C$ *i*-MXene layers (Fig. 1a and b). The as-prepared *i*-MXene-based fiber is favorable for transport and storage of charge due to its interconnected network architecture which is rich in mesopores. Fiber-type supercapacitors (FSCs) fabricated with these fibers is shown to provide a combination of high capacitance, high rate capabilities and excellent cycling stability. In addition, an asymmetric fiber-type device was constructed by using the $Mo_{1.33}C$/PEDOT:PSS hybrid fiber and rGO fiber, which can be used both for supercapacitors and electrochemical transistors (ECTs). The resulting asymmetric fiber type supercapacitor (AFSCs) is extremely flexible and can operate in a wide potential window of

1.6 V, with high capacitance, excellent rate and cycling stability, as well as with an improved energy density. Furthermore, the water-based *i*-MXene ECTs exhibit shorter switching time, higher transconductance and $I_{on/off}$ ratios, compared to pristine PEDOT:PSS. In this work, the multifunctional smart *i*-MXene fibers prepared by a scalable method suggest that they are promising candidates for high-performance, portable, flexible, and wearable electronics.

Experimental section

Materials synthesis

Synthesis of $Mo_{1.33}C$ *i*-MXene. The $Mo_{1.33}C$ *i*-MXene was synthesized by the previously reported method.[36] Simply, 1 g of *i*-MAX phase of $(Mo_{2/3}Sc_{1/3})_2AlC$ was added to 20 ml 48% HF, then stirring at room temperature for 24 h. The multilayer $Mo_{1.33}$ was washed by deionized water until the pH value of the supernatant reaches about 6, and thereafter intercalated with TBAOH. The dark green supernatant of delaminated $Mo_{1.33}$ solution was then centrifuged at 3000 rpm for 30 min to remove multilayer $Mo_{1.33}C$ *i*-MXene. The concentration of the $Mo_{1.33}C$ dispersion was measured by vacuum drying a specific volume of the colloidal solution.

Preparation of $Mo_{1.33}C$ *i*-MXene/PEDOT:PSS paste. For the $Mo_{1.33}C$/PEDOT:PSS hybrid fibers, the hybrid paste was first

prepared by mixing PEDOT:PSS and $Mo_{1.33}C$ ($\sim$7 mg ml^{-1}) dispersions. The mass ratio between $Mo_{1.33}C$ *i*-MXene (M) and PEDOT:PSS (P) was controlled to be 2 : 1. The mixture was stirred for 5 min and then dropped in 1 M H_2SO_4 solution. After centrifugation at 4000 rpm for 10 min, the hybrid paste was washed by deionized water 3 times.

Preparation of $Mo_{1.33}C$/PEDOT:PSS hybrid fibers. The hybrid paste was loaded into a 3 ml syringe with a blunt needle (inner diameter 300 μm) and mounted on a syringe pump. The paste was extruded at a flow rate of $\approx$5 ml h^{-1} into a bath of 1% PEI. The resulting fiber was washed by an ethanol/water mixture (volume ratio 1 : 4) and then dried by freeze drying. Based on the prepared fiber, the mass loading of the hybrid fiber electrodes is 24 mg cm^{-2} and the mass loading of the symmetric device is 36 mg cm^{-2}.

Preparation of rGO fibers. GO was prepared by using the modified Hummers' method as reported in our previous papers.[39] The fibers were prepared as hybrid fibers. The GO solution (10 mg ml^{-1}) was loaded into a 3 ml syringe with a blunt needle and was extruded into a bath of methanol solution with 3 M KCl. After freeze drying, the GO fibers were reduced by using hydroiodic acid as the reduction agent at 80 °C for 10 h.

Preparation of the gel electrolyte. 1 g of PVA (Sigma Aldrich, M_w 85 000–120 000) was added to 10 ml deionized water and was then stirred at 85 °C for 10 h until a clear solution was obtained. 1 g of H_2SO_4 was added to the solution and cooled down to room temperature and then stirred for 2 h.

Device assembly. The $Mo_{1.33}C$/PEDOT:PSS hybrid fiber and rGO fiber were placed closely and in parallel on a substrate (such as glass or PET), and then a thin layer of the PVA–H_2SO_4 gel electrolyte was applied on top of the fibers. The silver paste applied at both ends of the fibers served as the contact electrodes for electrochemical measurements. The fiber-shaped devices were placed in a fume hood to allow the gel electrolyte to solidify.

Characterization

The capacitor performance tests were performed using a VSP potentiostat (BioLogic, France). In the three-electrode configuration, the fiber was used as working electrode, a platinum foil as the counter electrode and Ag/AgCl in 1 M KCl as the reference electrode, using an aqueous solution containing H_2SO_4 (3 M) as the electrolyte. For the two-electrode symmetrical supercapacitor device, the *i*-MXene based hybrid fiber as both working electrodes and counter electrode. For AFSCs, the rGO fiber as the working electrodes and the *i*-MXene based hybrid fiber as counter electrode. The impedance measurements were performed at an open circuit potential with a 5 mV amplitude in a frequency range from 10 mHz to 100 kHz. The electrical characterization of the fiber type ECTs was carried out by means of a Keithley 4200 semiconductor parameter analyzer. The $Mo_{1.33}C$/PEDOT:PSS hybrid fiber was used as source and drain terminals and the rGO fiber as gate electrode. The transistor channel was defined by the contact area of the gel electrolyte with the source-drain fiber. The morphology of the fibers were carried out using SEM (LEO 1550 Gemini). XRD was carried out on a PANalytical X'Pert diffractometer using Cu Kα radiation (45 kV and 40 mA). Atomic force microscopy (AFM) was performed at ambient conditions (room temperature in a lab) using a Veeco DI Dimension 3100 scanning probe microscope, equipped with nanoscope IV electronics. The measurements were performed in tapping mode using Si tips (PPPNCHR-50 from Nanosensors) with a tip radius of curvature < 7 nm.

Results and discussion

The delaminated $Mo_{1.33}C$ *i*-MXene was obtained by selectively etching the Al and Sc from the *i*-MAX phase ($(Mo_{2/3}Sc_{1/3})_2AlC$), as reported previously.[36] The successful etching and exfoliation of the *i*-MAX phase is confirmed by the disappearance of the peak at $2\theta = 13.1°$ (*i*-MAX phase) and a new peak appearing at 7.2° (*i*-MXene) in the XRD pattern (Fig. S1†). As shown in the SEM image, the average lateral size of exfoliated $Mo_{1.33}C$ monolayers is around 1.3 μm (Fig. 1c). In addition, from atomic force microscopy (AFM) mapping it is revealed that the thickness of the $Mo_{1.33}C$ monolayers is around 1.2 nm (Fig. 1d), which is as expected and thinner compared to previously reported $Ti_3C_2T_z$ MXene.[29] The $Mo_{1.33}C$/PEDOT:PSS fiber prepared by the scalable wet-spinning method is schematically illustrated in Fig. 1b (see details in the Experimental section). Briefly, the fibers are produced through coagulation of $Mo_{1.33}C$/PEDOT:PSS paste in 1% polyethylenimine (PEI) solution where PEI with a rich ammonium end group, can act as a cross-linking polymer binding $Mo_{1.33}C$ and PEDOT:PSS to create a three-dimensional architecture within the fiber *via* self-assembling. To confirm that PEI, as a cross-linking agent, is involved in the self-assembly process of the fibers, FT-IR is performed as shown in Fig. 1e. The peak at 3310 cm^{-1} for PEI is produced by N–H vibrations of the terminal primary amine. This peak is retained in the fiber, which is direct evidence of PEI being involved in the fiber assembly. This method of cross-linker enable the fibers to exhibit high tensile strength (Fig. S2†). Scanning electron microscope (SEM) images show that the fiber has a porous relatively smooth outer wall that keeps the cylindrical structure from collapsing during the spinning process (Fig. 1f). The cross-section SEM images (Fig. 1g and h) of the fibers reveal that the 3D porous microstructure of the fibers is achieved by homogeneously dispersed $Mo_{1.33}C$ sheets and PEDOT:PSS. The $Mo_{1.33}C$/PEDOT:PSS fiber exhibited a micropore-dominated pore-size distribution, consistent with the result of N_2 adsorption–desorption (Fig. S3†). Within the hybrid fiber, the $Mo_{1.33}C$, which have a large surface area, offers a high capacitance and electrical conductivity, while the laminated *i*-MXene/polymer structure and 3D network architecture offers more active sites and ion transport channels. These synergistic effects contribute to the enhanced electrochemical performance achieved in the hybrid fibers.

The application of as-synthesized fibers in a capacitor was first studied in a three-electrode cell with a 3 M H_2SO_4 electrolyte. The pristine $Mo_{1.33}C$ film and PEDOT:PSS fibers were also investigated for reference (Fig. S4†). The cyclic voltammetry (CV) curves of the hybrid fibers for scan rates in the range 2–

12546 | *J. Mater. Chem. A*, 2022, **10**, 12544–12550
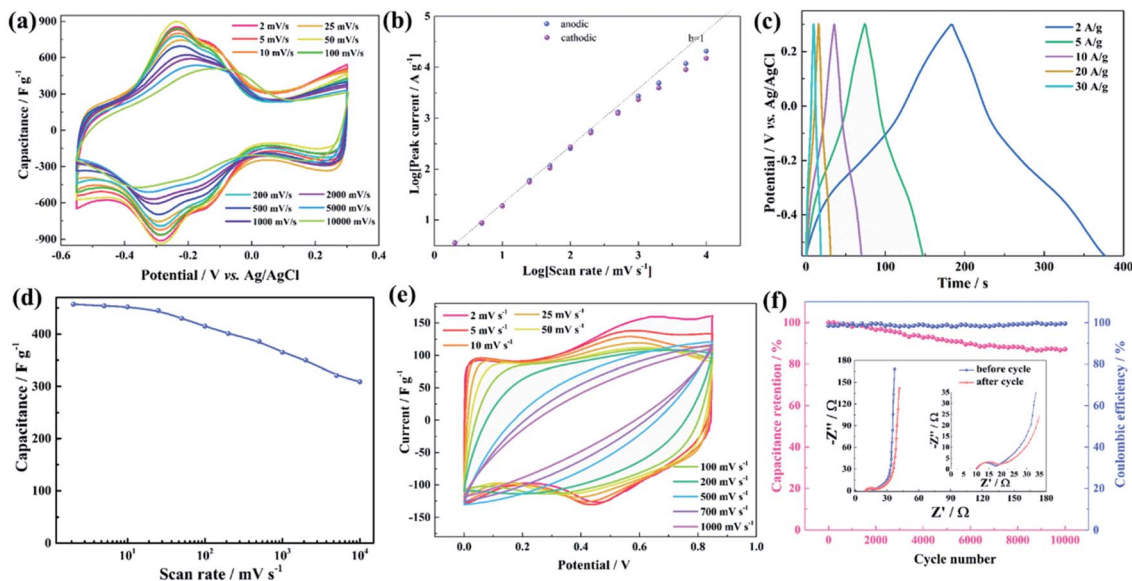
This journal is © The Royal Society of Chemistry 2022

Fig. 2 Electrochemical performance of hybrid fiber electrodes and devices. (a) CV curves of fiber electrodes at different scan rates. (b) Plot of the cathodic and anodic peak current against the scan rate for the fiber electrodes. (c) Galvanostatic charge−discharge (GCD) curves of fiber electrodes at different current densities. (d) Capacitance of fiber electrodes as a function of scan rate. (e) CV curves of the fiber based symmetrical supercapacitors at different scan rates. (f) Cycling stability of the fiber based symmetrical supercapacitors during 10 000 cycles at a rate of 20 A g^{-1}. Inset in (f) shows representative EIS curves before and after the cycling test.

10 000 mV s^{-1} revealed negligible distortion. As shown in Fig. 2a, the CV curves at low scan rate show reversible redox peaks at −0.3 to −0.2 V vs. Ag/AgCl. In addition, the small redox peaks in the range of −0.2 to −0.1 V (vs. Ag/AgCl) likely originates from traces of MoO$_3$. Even for a scan rate up to 10 000 mV s^{-1}, the pair of redox peaks persists, indicating excellent rate performance. To explore the charge storage kinetics, the relationship of cathodic and anodic peak current density against the scan rate is shown in Fig. 2b. The b-value obtained from the power-law (see ESI†) can directly reflect the charge storage kinetics. Herein, the fiber electrode exhibits predominantly surface reactions processes since the b value is close to 1 for a scan rate between 2 and 1000 mV s^{-1}. This can be understood by the 3D network architecture of the fiber significantly reducing the ion diffusion distance. In addition, the galvanostatic charge/discharge (GCD) curves of the fiber electrodes at different current densities are highly symmetrical with a low iR drop (∼0.08 V) even at a high discharge current density of 30 A g^{-1}, which confirm the high reversibility of the redox reactions and good Coulomb efficiency (Fig. 2c). The rate performance of the fiber electrodes is presented in Fig. 2d. The specific capacitance of the fiber electrodes decreased only slightly from 457 F g^{-1} to 309 F g^{-1} when the scan rate was increased from 2 to 10 000 mV s^{-1} (retention of 67.6%), the capacitance and retention of hybrid fiber electrode is surpasses the reported graphene, CNT or Ti$_3$T$_2$T$_z$ based fibers (Table S1†).[39,40] The excellent rate performance is consistent with the CV results, which can also be confirmed by electrochemical impedance spectroscopy (EIS, Fig. S5†).

To further explore the potential of fibers for energy storage, a flexible solid-state FSC is fabricated. The performance of the

FSC device is investigated through CV curves at different scan rate (Fig. 2e). Similar with the fiber electrodes, a pair of redox peaks appears in the CV curves of the FSC device at low scan rates, which indicates a low charge transfer resistance and good reversibility. However, the CV curves show serious distortion with the increase of the scan rate. This may be caused by incomplete ion migration in gel electrolyte based supercapacitor devices. Therefore, the redox peak disappeared when the scan rate increased up to 200 mV s^{-1}. The FSC device shows a capacitance of 110 F g^{-1} at a scan rate of 2 mV s^{-1} and remain above 61.3 F g^{-1} even at scan rates up to 1000 mV s^{-1} (Fig. S6†). The FSC device not only exhibits superior rate performance but also shows excellent cycling stability. After 10 000 cycles, a capacitance retention of 87% and coulombic efficiency of 99% are achieved at a rate of 20 A g^{-1} (Fig. 2f).

Encouraged by the excellent specific capacitance of the FSC described above, an asymmetric fiber type supercapacitor (AFSCs) was assembled using Mo$_{1.33}$C/PEDOT:PSS hybrid fiber and rGO fiber (Fig. S7–S9†) as the cathode and anode (Fig. 3a), respectively, which can further improve the energy density by widening the operating voltage. Notably, the AFSC achieve an operating potential window up to 1.6 V, which yields higher energy density compared to corresponding symmetric devices. The CV curves of the AFSCs at different scan rates showed excellent rate performance (Fig. 3b), showing negligible degradation up to 200 mV s^{-1}. The nearly symmetric GCD curves of the AFSC at different current density demonstrate fast ion and electron transfer kinetics, highly reversible redox processes, and high coulombic efficiency (Fig. 3c). The capacitance of the device reaches 105 F g^{-1} at a scan rate of 2 mV s^{-1} and maintains a capacitance of 54 F g^{-1} at a scan rate of 1000 mV s^{-1}
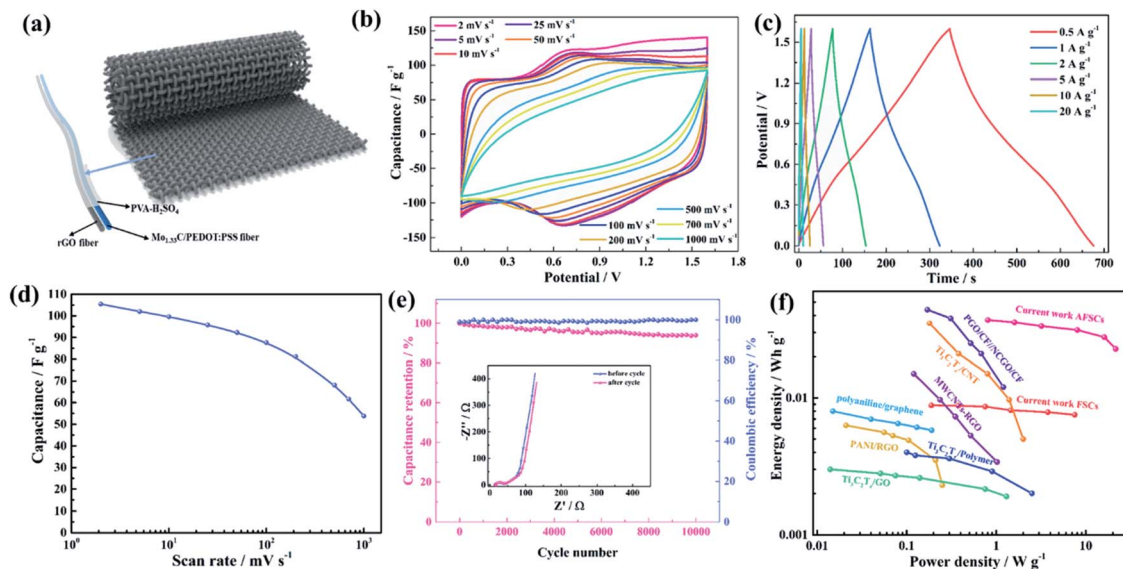
Fig. 3 Asymmetric fiber type supercapacitors (AFSCs) developed using MXene-based fibers as cathodes and rGO fibers as anode. (a) Schematic illustration of $Mo_{1.33}C$/PEDOT:PSS//rGO AFSCs woven into a textile. (b) CV curves of $Mo_{1.33}C$/PEDOT:PSS//rGO fiber-based supercapacitors at different scan rate. (c) GCD curves of AFSCs at different current densities. (d) Scan rate dependent capacitance of AFSCs. (e) Capacitance retention of AFSCs tested by galvanostatic cycling at 10 A g^{-1}. The Inset depicts the representative EIS curves before and after the cycling test. (f) Plot of energy density versus power density for our fiber-based supercapacitors and other reported fiber-based supercapacitors.

(Fig. 3d). In addition, the AFSC demonstrates excellent cycling stability, and a capacitive retention of 94% is achieved after 10 000 cycles by GCD tests at a current of 10 A g^{-1} (Fig. 3e). The EIS pattern, with almost negligible increase at the high frequencies before and after the cycles, shows that the internal resistance of the fiber electrode and gel electrolyte hardly
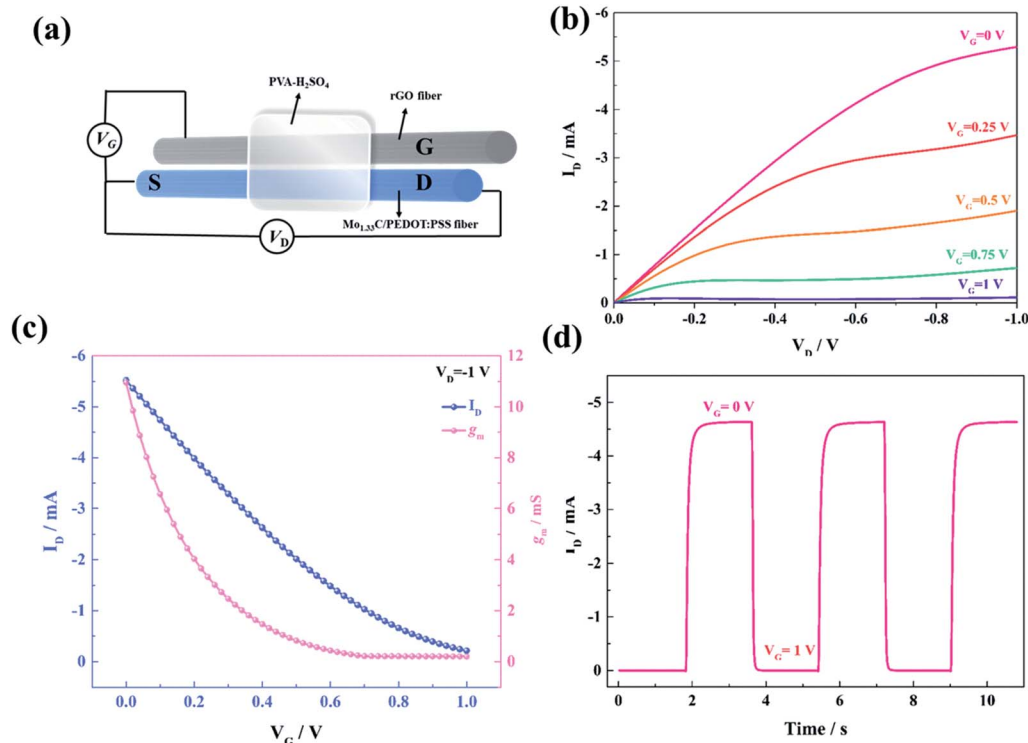

Fig. 4 Fiber type ECT developed using i-MXene-based fibers as source (S), drain (D) and rGO fibers as gate (G). (a) Schematic illustration of fiber type ECT. (b) Output characteristics of a fiber-based ECT showing the drain-source current I_D with respect to the drain-source voltage V_D. The gate voltage V_G was varied from 0 to 1.0 V. (c) Transfer characteristics of the same device and the corresponding transconductance (g_m) values at $V_D = -1$ V. (d) Corresponding transient characteristics showing I_D as a function of time t during repeated switching of V_G between 0 and 1.0 V.

12548 | J. Mater. Chem. A, 2022, 10, 12544–12550

This journal is © The Royal Society of Chemistry 2022

changes after cycling (Fig. 3e inset, Fig. S12†). This indicates that the 3D porous structure of the fiber electrode can effectively resist the influence of the electrode during the process of ion migration into and out of the electrode. At low frequency, a large slope is present in all fiber electrodes, which may be attributed to the ability of the 3D porous structure to maintain highly accessible surface before and after cycling. Furthermore, AFSCs are conveniently integrated in series and/or parallel configurations to increase the output voltage or total capacitance (Fig. S13†). The Ragone plots of the energy and power densities for the AFSCs are compared with those reported in the literatures.[21,41–46] As shown in Fig. 3f, the fiber-based asymmetric device is superior to the symmetric device. A maximum energy density of 37 mW h g^{-1} is reached at a power density of 805 mW g^{-1}. Notably, this energy density value is higher than those of recently reported fiber-based supercapacitors.[43–45] The outstanding performance of the $Mo_{1.33}C$/PEDOT:PSS fiber based supercapacitors originates from a high electrode conductivity, fast electrolyte diffusion kinetics provided by 3D network architecture, and a fast pseudocapacitive storage mechanism.

Electrochemical transistors (ECTs) have attracted great attention for flexible electronics and bioelectronics applications ranging from printable logic circuits for e-textiles to drivers for sensors and neuromorphic devices.[47–50] However, the channel components are mainly organic semiconductors or organic polyelectrolytes, while the research on inorganic semiconductor materials or organic-inorganic composite materials is sparse. In order to further expand the application field of $Mo_{1.33}C$/PEDOT:PSS fibers, a fiber type ECT was fabricated by a simple parallel configuration (Fig. 4a). The two ends of the $Mo_{1.33}C$/PEDOT:PSS fiber represented the ECT source and drain terminals, whereas the rGO fiber served as the gate electrode. Fig. 4 shows a typical set of output, transfer and transient curves of the fiber type ECT device. When a positive bias voltage is applied to the gate, the channel conductivity will decrease due to dedoping, and thus reduce the drain-source current (I_D). As shown in Fig. 4b, the output characteristics of the device show saturation of I_D with increasing drain-source voltage (V_D) and operates at low gate voltages ($V_G < 1.0$ V). At the same time, the device shows a large transconductance of 10.8 mS (Fig. 4c). The fiber type ECT shows a switching behavior from ON to OFF as the gate voltage pulses from $V_G = 0$ to 1 V (Fig. 4d). The response time of this fiber type ECT is 0.1 and 0.03 s for the switch on and switch off, respectively. These values are better than that of planar ECT of PEDOT:PSS (Fig. S14†). Considering that ECT operation must rely on both electron and ion transport, all the results suggest that the $Mo_{1.33}C$/PEDOT:PSS fiber have a good balance/optimization of these two processes, that is, the 3D composite network architecture has excellent electron and ion transport kinetics.

Conclusions

In summary, we demonstrate a scalable strategy to realize a multifunctional flexible i-MXene based smart fiber by spinning $Mo_{1.33}C$/PEDOT:PSS hybrid paste from PEI solution, which is simple, efficient, and easily scaled up for mass production. The as-prepared i-MXene fibers, with high electrochemical activity and interconnected 3D network architecture, is beneficial for both electron and ion transport and storage. A solid-state, fiber-based asymmetric device was fabricated by using $Mo_{1.33}C$/PEDOT:PSS fiber and rGO fiber, which can be used for both supercapacitors and electrochemical transistors, ECT. The asymmetric fiber type supercapacitor, AFSC, with an operating potential window of 1.6 V, showed a high energy density (37 mW h g^{-1}), a high capacitance retention and cycling stability. The resulting fiber type ECT exhibits fast ion intercalation/de-intercalation, high transconductance and short response time. The here presented design strategies for multifunctional fiber devices show potential for applications in wearable and portable electronics.

Author contributions

Leiqiang Qin and Jianxia Jiang conducted the materials synthesis and the structural and electrochemical characterization. Leiqiang Qin, and Johanna Rosen analyzed the experimental data. Leiqiang Qin, Fengling Zhang and Lintao Hou prepared the manuscript. Johanna Rosen supervised the project and co-wrote the manuscript. All the authors discussed the results and contributed to writing the manuscript.

Conflicts of interest

The authors declare that they do not have any conflicts of interest.

Acknowledgements

References

1 J. Liu, M. A. G. Namboothiry and D. L. Carroll, *Appl. Phys. Lett.*, 2007, **90**, 063501.

2 B. O'Connor, K. P. Pipe and M. Shtein, *Appl. Phys. Lett.*, 2008, **92**, 193306.

3 M. R. Lee, R. D. Eckert, K. Forberich, G. Dennler, C. J. Brabec and R. A. Gaudiana, *Science*, 2009, **324**, 232–235.

4 J. Pu, K. Zhang, Z. Wang, C. Li, K. Zhu, Y. Yao and G. Hong, *Adv. Funct. Mater.*, 2021, **31**, 2106315.

This journal is © The Royal Society of Chemistry 2022

J. Mater. Chem. A, 2022, **10**, 12544–12550 | **12549**

5   L. Li, Q. Zhang, B. He, R. Pan, Z. Wang, M. Chen, Z. Wang, K. Yin, Y. Yao, L. Wei and L. Sun, *Adv. Mater.*, 2022, **34**, 2104327.

6   M. Maccioni, E. Orgiu, P. Cosseddu, S. Locci and A. Bonfiglio, *Appl. Phys. Lett.*, 2006, **89**, 143515.

7   Q. Zhang, L. Li, H. Li, L. Tang, B. He, C. Li, Z. Pan, Z. Zhou, Q. Li, J. Sun, L. Wei, X. Fan, T. Zhang and Y. Yao, *Nano Energy*, 2019, **60**, 267–274.

8   M. Hamedi, L. Herlogsson, X. Crispin, R. Marcilla, M. Berggren and O. Inganäs, *Adv. Mater.*, 2009, **21**, 573–577.

9   O. C. Compton and S. T. Nguyen, *Small*, 2010, **6**, 711–723.

10 R. Mas-Balleste, C. Gomez-Navarro, J. Gomez-Herrero and F. Zamora, *Nanoscale*, 2011, **3**, 20–30.

11 J. Liu, H.-B. Zhang, R. Sun, Y. Liu, Z. Liu, A. Zhou and Z.-Z. Yu, *Adv. Mater.*, 2017, **29**, 1702364.

12 N. Kurra, B. Ahmed, Y. Gogotsi and H. N. Alshareef, *Adv. Energy Mater.*, 2016, **6**, 1601372.

13 Z. Dong, C. Jiang, H. Chen, Y. Zhao, G. Shi, L. Jiang and L. Qu, *Adv. Mater.*, 2012, **24**, 1856–1861.

14 A. B. Dalton, S. Collins, E. Munoz, J. M. Razal, V. H. Ebron, J. P. Ferrais, J. N. Coleman, B. G. Kim and R. H. Baughman, *Nature*, 2003, **423**, 703.

15 X. Chen, L. Qiu, J. Ren, G. Guan, H. Lin, Z. Zhang, P. Chen, Y. Wang and H. Peng, *Adv. Mater.*, 2013, **25**, 6436–6441.

16 Z. Zhou, W. Panatdasirisuk, T. S. Mathis, B. Anasori, C. Lu, X. Zhang, Z. Liao, Y. Gogotsi and S. Yang, *Nanoscale*, 2018, **10**, 6005–6013.

17 L. Kou, T. Huang, B. Zheng, Y. Han, X. Zhao, K. Gopalsamy, H. Sun and C. Gao, *Nat. Commun.*, 2014, **5**, 3754.

18 S. H. Aboutalebi, R. Jalili, D. Esrafilzadeh, M. Salari, Z. Gholamvand, S. A. Yamini, K. Konstantinov, R. L. Shepherd, J. Chen, S. E. Moulton, P. C. Innis, A. I. Minett, J. M. Razal and G. G. Wallace, *ACS Nano*, 2014, **8**, 2456–2466.

19 L. Liu, Y. Yu, C. Yan, K. Li and Z. Zheng, *Nat. Commun.*, 2015, **6**, 7260.

20 Y. Meng, Y. Zhao, C. Hu, H. Cheng, Y. Hu, Z. Zhang, G. Shi and L. Qu, *Adv. Mater.*, 2013, **25**, 2326–2331.

21 S. Seyedin, E. R. S. Yanza and J. M. Razal, *J. Mater. Chem. A*, 2017, **5**, 24076–24082.

22 G. Sun, X. Zhang, R. Lin, J. Yang, H. Zhang and P. Chen, *Angew. Chem., Int. Ed.*, 2015, **54**, 4651–4656.

23 N. Yu, H. Yin, W. Zhang, Y. Liu, Z. Tang and M.-Q. Zhu, *Adv. Energy Mater.*, 2016, **6**, 1501458.

24 J. Xu, Q. Wang, X. Wang, Q. Xiang, B. Liang, D. Chen and G. Shen, *ACS Nano*, 2013, **7**, 5453–5462.

25 S. Zhai, C. Wang, H. E. Karahan, Y. Wang, X. Chen, X. Sui, Q. Huang, X. Liao, X. Wang and Y. Chen, *Small*, 2018, **14**, 1800582.

26 Q. Jiang, N. Kurra, M. Alhabeb, Y. Gogotsi and H. N. Alshareef, *Adv. Energy Mater.*, 2018, **8**, 1703043.

27 X. Yang, Q. Wang, K. Zhu, K. Ye, G. Wang, D. Cao and J. Yan, *Adv. Funct. Mater.*, 2021, **31**, 2101087.

28 M. Naguib, M. Kurtoglu, V. Presser, J. Lu, J. Niu, M. Heon, L. Hultman, Y. Gogotsi and M. W. Barsoum, *Adv. Mater.*, 2011, **23**, 4248–4253.

29 L. Qin, J. Jiang, Q. Tao, C. Wang, I. Persson, M. Fahlman, P. O. Å. Persson, L. Hou, J. Rosen and F. Zhang, *J. Mater. Chem. A*, 2020, **8**, 5467–5475.

30 J. Chen, M. Chen, W. Zhou, X. Xu, B. Liu, W. Zhang and C. Wong, *ACS Nano*, 2022, **16**, 2461–2470.

31 X. Yang, Y. Yao, Q. Wang, K. Zhu, K. Ye, G. Wang, D. Cao and J. Yan, *Adv. Funct. Mater.*, 2022, **32**, 2109479.

32 J. Jiang, L. Qin, J. Halim, P. O. A. Persson, L. Hou and J. Rosen, *Nano Res.*, 2021, **15**, 3587–3593.

33 A. VahidMohammadi, J. Rosen and Y. Gogotsi, *Science*, 2021, **372**, 6547.

34 M. Naguib, O. Mashtalir, J. Carle, V. Presser, J. Lu, L. Hultman, Y. Gogotsi and M. W. Barsoum, *ACS Nano*, 2012, **6**, 1322–1332.

35 M. Naguib, J. Halim, J. Lu, K. M. Cook, L. Hultman, Y. Gogotsi and M. W. Barsoum, *J. Am. Chem. Soc.*, 2013, **135**, 15966–15969.

36 Q. Tao, M. Dahlqvist, J. Lu, S. Kota, R. Meshkian, J. Halim, J. Palisaitis, L. Hultman, M. W. Barsoum, P. O. Å. Persson and J. Rosen, *Nat. Commun.*, 2017, **8**, 14949.

37 L. Qin, Q. Tao, A. Ghazaly, J. Fernández-Rodríguez, P. O. Å. Persson, J. Rosen and F. Zhang, *Adv. Funct. Mater.*, 2018, **28**, 1703808.

38 B. Ahmed, A. Ghazaly and J. Rosen, *Adv. Funct. Mater.*, 2020, **30**, 2000894.

39 Y. Li, Y. Zhao, H. Cheng, Y. Hu, G. Shi, L. Dai and L. Qu, *J. Am. Chem. Soc.*, 2012, **134**, 15–18.

40 Z. Bo, W. Zhu, W. Ma, Z. Wen, X. Shuai, J. Chen, J. Yan, Z. Wang, K. Cen and X. Feng, *Adv. Mater.*, 2013, **25**, 5799–5806.

41 M. Acerce, D. Voiry and M. Chhowalla, *Nat. Nanotechnol.*, 2015, **10**, 313–318.

42 P. Li, Z. Jin, L. Peng, F. Zhao, D. Xiao, Y. Jin and G. Yu, *Adv. Mater.*, 2018, **30**, 1800124.

43 C. Zhou, T. Gao, Y. Wang, Q. Liu, Z. Huang, X. Liu, M. Qing and D. Xiao, *Small*, 2019, **15**, 1803469.

44 T. Ni, S. Wang, J. Shi, X. Du, Q. Cheng, Z. Dong, L. Ruan, W. Zeng, X. Guo, X. Ren and Z. Huang, *Adv. Mater. Technol.*, 2020, **5**, 2000268.

45 X. Zheng, L. Yao, Y. Qiu, S. Wang and K. Zhang, *ACS Appl. Energy Mater.*, 2019, **2**, 4335–4344.

46 J. Zhang, S. Seyedin, S. Qin, Z. Wang, S. Moradi, F. Yang, P. A. Lynch, W. Yang, J. Liu, X. Wang and J. M. Razal, *Small*, 2019, **15**, 1804732.

47 Z. Wang, S. Qin, S. Seyedin, J. Zhang, J. Wang, A. Levitt, N. Li, C. Haines, R. Ovalle-Robles, W. Lei, Y. Gogotsi, R. H. Baughman and J. M. Razal, *Small*, 2018, **14**, 1802225.

48 S. Fabiano, N. Sani, J. Kawahara, L. Kergoat, J. Nissa, I. Engquist, X. Crispin and M. Berggren, *Sci. Adv.*, 2017, **3**, e1700345.

49 Y. van de Burgt, E. Lubberman, E. J. Fuller, S. T. Keene, G. C. Faria, S. Agarwal, M. J. Marinella, A. A. Talin and A. Salleo, *Nat. Mater.*, 2017, **16**, 414–418.

50 P. Gkoupidenis, D. A. Koutsouras and G. G. Malliaras, *Nat. Commun.*, 2017, **8**, 15448.